Creation of a dual-porosity micromodel for pore-level visualization of multiphase flow

M. Buchgraber, M. Al-Dossary [1], C.M. Ross, A.R. Kovscek *

Department of Energy Resources Engineering, Stanford University, Stanford, CA 94305, USA

ARTICLE INFO

ABSTRACT

This paper describes the creation and testing of an etched-silicon micromodel that has the features and characteristics of a dual-porosity pore system mimicking those found in certain carbonate reservoir rocks. This micromodel consists of a two-dimensional (2D) pore network etched into a silicon wafer with a bonded glass cover that permits direct visual examination of pore-level displacement mechanisms and pore-network characteristics during fluid flow experiments. The approach began by creating a mosaic of images from a carbonate thin section of a sample with both high porosity and permeability using a scanning electron microscope (SEM) in back-scattered mode (BSE). Connections based on high-pressure mercury injection data were made to ensure that the 2D connectivity in the imaged pore structure was representative of the three dimensional (3D) pore network of the carbonate sample. Microelectronic photolithography techniques were then adapted to create micromodels for subsequent fluid flow experiments. Micromodel surfaces were made oil- or water-wet by various techniques. One of the main advantages of having a representative carbonate dual-porosity micromodel is the ability to observe pore-level mechanisms of multiphase flow and interpret petrophysical properties. Another advantage is that multiple replicates are available with identical conditions for each new experiment. Micromodel utility is demonstrated here through the measurement of porosity, permeability, fluid desaturation patterns, and recovery factors.

© 2012 Elsevier B.V. All rights reserved.

1. Introduction

Microporosity can be a significant porosity type in carbonate reservoirs. Micropores or pores that are 10 μm or less in diameter in the Middle Eastern Arab-D reservoir quality rock comprise 25% to as much as 50% of the total porosity (Cantrell and Hagerty, 1999). The abundance of microporosity has significant implications for fluid flow properties as well as for the distribution of fluids and sometimes leads to misinterpretation of log response. There is also a strong relationship between pore types, their distribution, and sizes as well as pore throat sizes associated with each given pore type (Ross et al., 1995). Direct pore-level observation of displacement mechanisms improves our understanding of two-phase flow behavior and petrophysical properties that depend strongly on the pore network structure (Oren et al., 1992).

This paper reports the creation of a dual-porosity micromodel that simulates typical Arab-D carbonates including microporosity. The task is more difficult with carbonate rocks, in comparison to sandstones. Carbonates tend to show a variety of length scales with some correlation among the pore and throat sizes and pore shapes (Ross et al., 1995). We attempt to understand further the key

components of a rock's pore system which impact multiphase flow behavior and, hence, the petrophysical properties.

The paper starts with an overview of microporosity types and their significance. Next, the methodology is given for the creation and development of the carbonate micromodel mask and etched-silicon micromodels. A first step is to mosaic and modify SEM BSE micrographs from an epoxy-impregnated thin section. Next, the apparatus and procedures used during the experiment are presented. The petrophysical characterization of the carbonate micromodel follows. A summary completes the paper.

2. Microporosity

Before discussing the geologic features of Arab-D reservoir rocks and our carbonate thin section, a definition for microporosity is needed as there are multiple definitions. For example, microporosity in carbonate rocks was defined by Choquette and Pray (1970) as any pore less than 62.5 μm in diameter, whereas Pittman's (1971) definition has a threshold less than 1 μm in size. For the design of our carbonate micromodel, however, we use the definition of Cantrell and Hagerty (1999) in which micropores are 10 μm or less in diameter.

The Arab-D Member is part of the Jurassic Arab Formation that consists mainly of skeletal and non-skeletal grainstones and packstones sealed with an impermeable anhydrite layer. Producing from the Arab-D interval, Ghawar is the largest oil field in the world at

* Corresponding author. Tel.: +1 650 723 1218; fax: +1 650 725 2099.
E-mail address: Kovscek@stanford.edu (A.R. Kovscek).
[1] Currently at Saudi Aramco.

1260 square miles. It currently produces 5 million barrels of oil per day (6.25% of global production) and its total estimated reserves are around 70 billion barrels of oil (US EIA, 2011).

Microporosity in the Arab-D Member contributes a quarter to half of the total core porosity (Cantrell and Hagerty, 1999). This microporosity exists as microporous grains, microporous matrix, microporous fibrous to bladed cements, and microporous equant cements (Cantrell and Hagerty, 1999). Microporous grains contribute the "most volumetrically significant microporosity type" in the Arab carbonates (Cantrell and Hagerty, 1999). Micropores are observed in most skeletal and non-skeletal grain types. SEM examination reveals that microporosity within grains occurs as pores 0.3 to 3.0 μm in diameter and is highly interconnected by uniform-sized straight tubular to laminar pore throats as determined using epoxy pore casts (Cantrell and Hagerty, 1999). Given the abundance of intragranular porosity in the Arab-D formation, microporous grains and, to a lesser extent, interparticle micropores are incorporated in the micromodel design.

Microporosity has direct and indirect implications on fluid flow properties and fluid distribution. Microporosity is also relevant to wireline log interpretation in that calculations of producible water saturations are sometimes too high. For example, micropores are usually filled with capillary-bound water while macropores are filled with oil for mixed-wet reservoir rocks. This gives a high water saturation response and may lead to a decision of not producing the interval, even though most of the water is immobile and only the oil filling the macropores flows (Petricola and Watfa, 1995).

According to Chilinger and Yen (1983), 80% of carbonate oil reservoirs are oil-wet, while 12% are intermediate-wet and 8% are water-wet. Furthermore, literature on Arab-D carbonate wettability found that Arab-D rocks exhibit neutral to oil-wet properties (Clerke, 2009).

3. Micromodels

A typical micromodel consists of a silicon wafer in which the image of a pore network is etched to a certain depth (say 20 μm) and bonded to a glass wafer (e.g., Rangel-German and Kovscek, 2006). The concept of developing micromodels has been around for decades, and most early micromodels were etched glass with uniform mesh pore geometry (Mattax and Kyte, 1961). Due to the drawbacks of such micromodels including concave shaped pore walls during the etching process, a new technique was developed whereby a photoresist was used to coat the glass, a network pattern was exposed selectively removing the photoresist, and the glass was etched where the photoresist was removed (Davis and Jones, 1968). This technique showed better pore geometry representation (Chambers and Radke, 1989). In cross section, however, this technique results in pores that are mainly eye shaped.

The pore networks and structures incorporated into a micromodel are typically created in one of two ways: (1) by analyzing thin section images or (2) by process-based analysis. McKellar and Wardlaw (1982) used a photo-imaging technique of thin sections followed by chemical etching of glass to produce micromodels. The first silicon micromodel replicated the pore body and throat sizes of a Berea sandstone pore network (Hornbrook, et al., 1991).

Currently, micromodels are made from silicon wafers and glass plates. The attraction of silicon is that the etching process is more controllable, more precise, and small-scale pore structures can be represented. This results in the ability to etch more complex and multifaceted pore network structures that are more similar to real pore structures found in reservoir rocks.

3.1. Mask creation

Micromodel fabrication starts by defining a base image that undergoes some digital modification to improve pore network
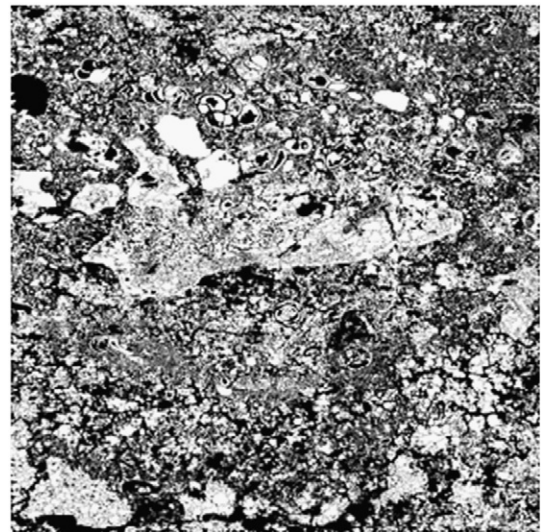

Fig. 1. Carbonate micromodel base image generated by creating a mosaic of SEM EDS gray scale images, 250×. Black represents epoxy-filled pores and white represents rock matrix.

connectivity and allow for seamless overlap of the edges. Once the base image is completed, it is used for mask preparation. The modified base image serves as a unit cell that is repeated or arrayed to fill the pore network portion of the micromodel. The number of repeats used in the array depends upon the size of the base image as well as the desired size of the micromodel. In this case, a three by three matrix was used.

The base image for our Arab-D proxy micromodel was collected using a JEOL JSM-5600LV SEM in BSE mode. An epoxy-impregnated thin section was imaged using overlapping views at a magnification of 250× (Fig. 1). Each SEM image is 2048 by 1600 pixels with a pixel size of 0.235 μm. The resulting composite or mosaicked image has dimensions of 10,065 by 13,407 pixels that represent a thin section area of 2.4 by 3.15 mm. The resulting image is 135 megapixels. The pixel size was increased later during the mask preparation due to resolution limitations of the mask making system.
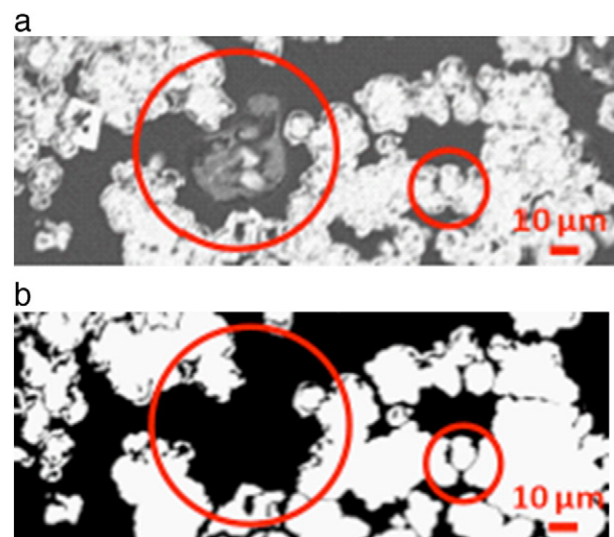

Fig. 2. Example views from (a) carbonate micromodel base image and (b) modified binary image. Red circles highlight where areas of incomplete epoxy impregnation were filled and pores isolated in 2D were reconnected. Black (or gray) represents epoxy-filled pores and white represents rock matrix.

Once the mosaic was constructed, it was converted to a binary image. In BSE images, gray-scale values correlate to average atomic number values that provide contrast between mineral and epoxy-filled regions. Thresholding the gray scale values produces a binary image in which black pixels correspond to the epoxy-filled pores whereas the white pixels represent the rock matrix. Further modifications were performed by hand to correct areas of incomplete epoxy impregnation, reconnect pores isolated in the 2D image, and erase regions obstructed with pore-filling gypsum cements (Fig. 2). In regions with incomplete impregnation, the areas are painted black for porosity unless particles intersect the uppermost plane of the thin section. Epoxy-filled pores that are isolated in the 2D base image are reconnected with throat-sizes derived from mercury injection data measured at pressures up to 33,000 psi (not shown). The presence of epoxy in the isolated pores indicates that they are connected in 3D. Also, the edges of the base image were modified to allow for seamless overlap during the array process and ensure flow conductivity between the arrayed images.

After the work of digitizing and modifying the base image was finished and the optimal array pattern had been selected, the mask preparation process continued. The base image was arrayed three times in both vertical and horizontal directions to fill a matrix area of 5 by 5.3 cm. Channels were added along the entire length of the inlet and production sides of the micromodel. These channels improve flow communication and provide a linear flow boundary condition rather than a point boundary condition. Each channel is connected to two ports that allow fluids to be either injected or produced from the micromodel. The repeated pattern image was then used, essentially, to create a photographic negative picture depicted on a chrome glass mask. Only one mask is needed for producing an endless supply of micromodels.

Complications arose due to machine limitations for writing the mask in that the system has a guaranteed minimum write dimension of 1.5 μm whereas our smallest size in the base image is 0.235 μm. This problem was overcome by converting the pixel size from 0.235 μm to 1.5 μm thereby retaining the heterogeneity and relative
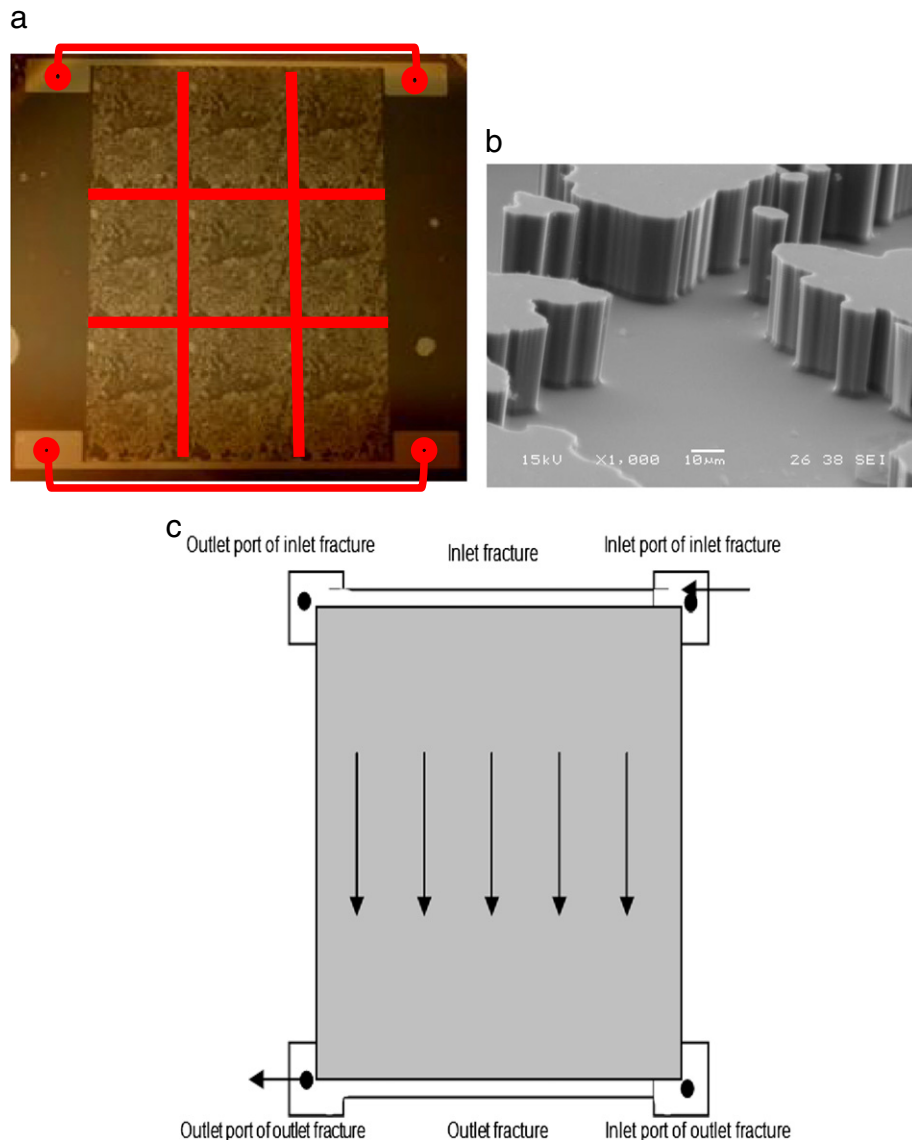

Fig. 3. (a) Carbonate-based chrome-quartz mask with nine repeated base images, injection and production ports, and communication fractures or channels outlined in red; (b) SEM micrograph of etched silicon wafer at 1000×; (c) Typical flow direction schematic for micromodels.

pore size distribution compared to other options such as resampling. The base image will be used in the future when technology allows for the base image to be written such that it preserves its high resolution and matrix size. Fig. 3 shows the carbonate pore structure mask with the nine repeated base images with four ports (inlet and production) and the two flow-distribution channels as well as a flow direction schematic and an SEM image of the etched-silicon wafer.

3.2. Micromodel fabrication

Micromodel fabrication occurred at the Stanford Nanofabrication Facility (SNF). It has a clean room equipped with machines and tools used to fabricate micro and nano devices (http://snf.stanford.edu). The fabrication process includes etching, cleaning, and bonding and it is presented schematically in Fig. 4. The steps in the fabrication process are the same for each micromodel; only the duration of certain steps is changed depending on the desired etch depth.

The imaging process begins by spin coating uniformly the type K-test silicon wafer with a Shipley 3612 photoresist layer that is 2 μm thick. One quality control action is to make sure that the wafers are dry and no moisture is present before the coating begins. If the wafers are suspected of being wet, they are "cooked" for 20 min at a temperature of 150 °C in a singe oven. After the wafers are coated, the mask is placed over the wafer and the assembly is exposed to ultra-violet (UV) light. Then, the excess photoresist is removed and the wafers are ready to be etched. Hydrofluoric acid gasses etch the regions exposed to UV light to the desired depth. The micromodels used in this study have etch depths of 5, 12, 14, 18, and 25 μm; however, most experiments were completed with a 25 μm ± 2 μm depth. A special tool, known as the Zygo White-Light 3D Surface Profiler, was used to verify the etching depths especially before depth sensitive measurements such as micromodel permeability. The Zygo has the ability to characterize and quantify the surface topographical characteristics. (Fig. 5; http://snf.stanford.edu/Equipment/EquipByName.html)

After the wafers are etched, holes for the four ports used for the inlets and outlets are drilled through the wafer. Wafers then undergo an intensive cleaning process to make sure that no remaining
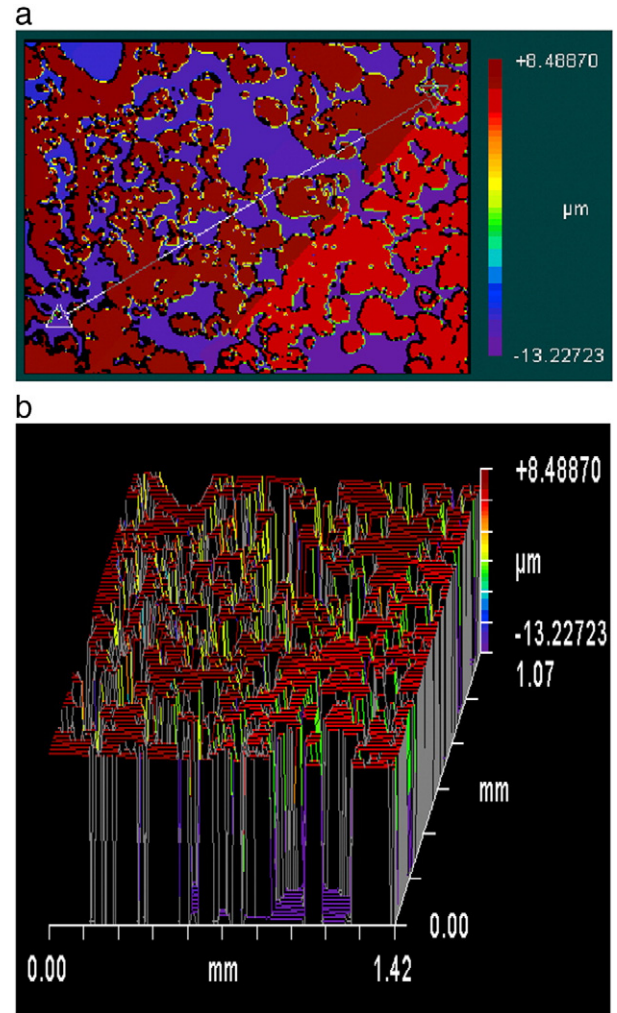

Fig. 5. Zygo profilometry measurement for quality control: (a) top view and (b) side view. Negative values indicate etched channels.
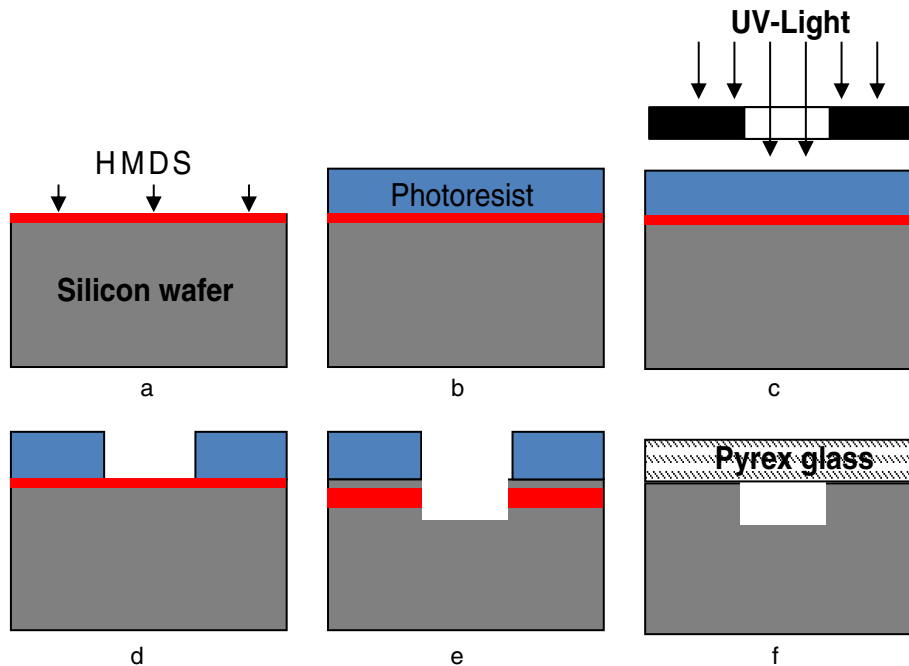

Fig. 4. Micromodel fabrication process: (a) vapor prime HMDS coating, (b) photoresist coating (1.6 μm), (c) contact alignment using the mask, (d) developing, (e) etching, and (f) anodic bonding.

photoresist and precipitated particles are present. To do so, the wafers are cleaned by immersing them in piranha, that is a heated solution consisting of sulphuric acid and hydrogen peroxide (9:1 H_2SO_4:H_2O_2), for 20 min.

The last step of the fabrication process is the bonding (Fig. 4). At this stage, the silicon wafers are etched and depict a pore network structure, but they are open on the top. A wafer is bonded anodically to a 500 μm thick, optically flat, borosilicate (Pyrex) glass cover plate that has a similar thermal expansion coefficient as the silicon. To achieve this, a silicon wafer is placed on top of a temperature-controlled hot plate at 700 °F for 30 min. During heating, the silicon surfaces of the wafer are oxidized. Once heated, the glass plate is placed on the micromodel and a roughly 1000 V potential is applied to complete the bonding. More details of bonding are discussed elsewhere (George, 1999; George et al., 2005).

3.3. Wettability alteration

Neinhuis and Barthlott (1997) showed that the hydrophobicity of a solid surface is governed by the chemical composition and microstructure of the surface. In our attempt to change micromodel wettability from water to oil wet, we tried various techniques. One successful method adapted a process described by Rao et al. (2010) where the micromodel is immersed in a solution that is 10% by volume of hexadecyltrimethylammonium bromide ($C_{19}H_{42}BrN$) in hexane solvent for 24 h. Heating then occurs at 100 °C and 150 °C for 1 h each. This technique needed some fine tuning to avoid foam formation and accumulation within the micromodel when water is injected and mixes with any residual solution. Foaming tends to plug the smallest pore throats.

It was also noticed during testing that the wettability of a micromodel changed as a result of being flooded with crude oil and aged with no initial water saturation. Presumably crude-oil components, such as asphaltenes and maltenes, adsorb to the solid thereby changing wettability in the absence of an aqueous phase (Kovscek et al., 1993). Wettability alteration persisted from test to test provided that micromodels were not cleaned with toluene or other harsh solvents. In the event of cleaning, retreatment with crude oil reestablished oil-wet conditions.

For both methods of wettability alteration, the technique used to observe the successfulness of the wettability alteration is visual analysis of the oil and water phase distributions at the pore-level under the microscope. Fig. 6 shows the micromodel with hydrophobic surfaces. Water is lightly shaded and is found to be disconnected, trapped, and surrounded by continuous oil phase. These observations are consistent with a surface that is oil wet (Kovscek et al., 1993). Given the somewhat simpler crude-oil treatment procedure, it was adopted as the method of choice for wettability alteration.

4. Experimental apparatus and procedures

This section provides a general overview of the tools, equipment, and procedures used to conduct flow experiments. The experimental set-up typically includes a syringe pump, pressure vessels as fluid containers, and a digital video camera for recording images.

A model 100D Teledyne ISCO syringe pump was used either for water injection immediately to the micromodel or for pushing water into pressure-transfer vessels to displace the fluids inside the vessels. Only deionized water is ever placed in the pump. The fluid transfer vessels used are steel piston and cylinders that are attached vertically to a holder for stability. The fluid supply and production tubes used during the experiments are transparent 1/8″ Teflon that are attached to the vessels. The microscope is a Nikon Eclipse ME 600. A Sony HDR-CX150 camcorder was mounted to the microscope using an adapter. Pictures and video were collected and then analyzed using image analysis tools.
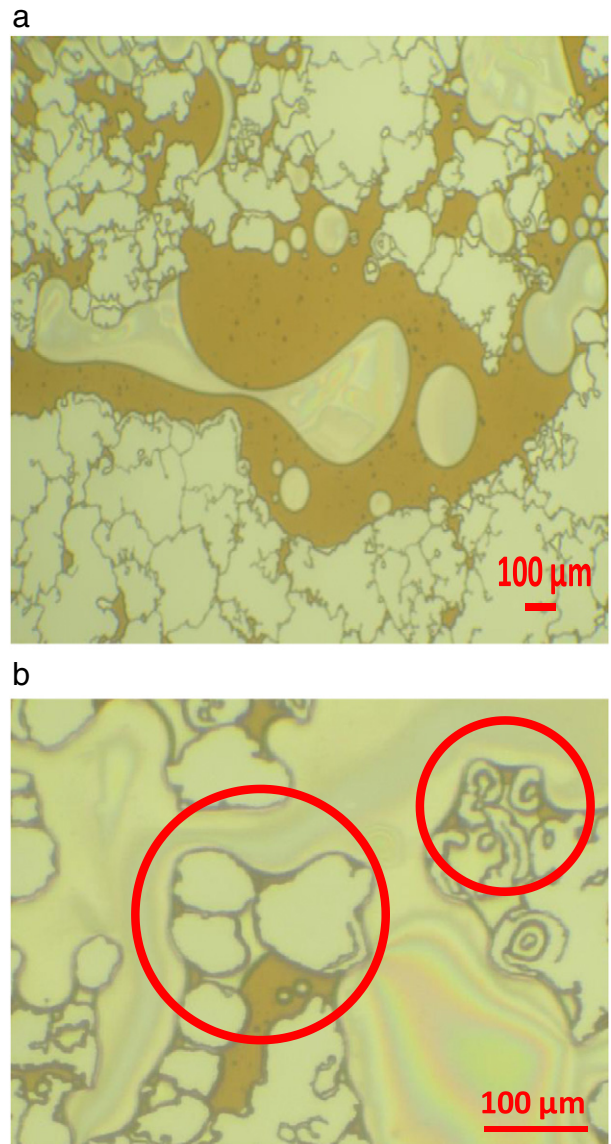
Fig. 6. Wettability altered micromodel with (a) water bubbles trapped in oil and (b) oil film (circled) that is coating the grains.

4.1. Micromodel holder

All experiments were conducted in a pressure range of 0 to 130 psi. Therefore, a regular low pressure micromodel holder was used. The holder provides a means to inject and produce fluids through the ports incorporated in the micromodel. The micromodel holder consists of two aluminum plates. This micromodel holder has four fluid entry and production ports that align with the ports on the micromodel. To seal properly the micromodel, O-rings are used around the fluid injection and production ports. The two halves of the holder are attached with eight screws. During the experiments, fluids are injected into the micromodel through one of the four ports. Fluids first fill the port volumes as well as the O-ring pool before reaching the micromodel, thereby contributing some dead fluid volume.

4.2. Procedures

Before starting the experiment, both the micromodel and micromodel holder have to be cleaned. If a complete cleaning is needed, the process starts by flushing the micromodel and its holder with

isopropanol (IPA) at a constant pressure drop of 50 psi. Then toluene is pumped also at constant pressure drop of 50 psi until no significant residual debris are noted. After that, CO_2 is injected to get rid of toluene. If after CO_2 injection, toluene appears to still occupy some of the micromodel pore space, the micromodel is subjected to vacuum pump and a heat lamp to evaporate any remaining toluene.

Water (or crude oil) was injected with a constant pressure drop of 10 to 120 psi into the micromodel in order to check if liquid completely filled the micromodel pore space. The micromodel is examined under the microscope at multiple locations until it is found to be 100% saturated. One aspect to note is that the water (or oil) injection time is extended for several hours after breakthrough to ensure no CO_2 bubbles are present inside the pore space. Back pressure is increased slightly to drive CO_2 into solution. Generally, it is found that either fluid (water or oil) is able to saturate fully a micromodel with the above procedure provided that the micromodel is well-etched and the quality control procedures were followed.

4.3. Image analysis

All of the pictures collected throughout the experiments were analyzed using image analysis to determine the micromodel porosity, saturations, recovery factors, and flow patterns. The image analysis method is required because of difficulties associated with performing accurate material balance calculations. For example, the micromodel etched to 25 μm with an average porosity of 46% has a pore volume (PV) of about 0.0294 mL. Each of the four ports has a volume of about 0.1 mL. Most of the volume of the micromodel is occupied by the four ports and the machined O-ring grooves. Any material balance calculation is, accordingly, difficult.

In the image analysis method, the pore structure is divided into a defined number of boxes, pictures are taken using the high resolution camera, and analysis is conducted using photostudio software. During our experiments, G.I.M.P. 2.6.0, a photo editing software, was used (www.gimp.org) to convert the images to black and white based on a chosen threshold value between 0 and 255 for the composite color image. A frequency versus intensity plot and a preview image are utilized to define the threshold value. After setting the threshold, all pixels having a lower intensity are converted to black pixels and pixels having greater intensity are converted to white pixels. Afterwards the histogram of the resulting black and white image is utilized to obtain the phase saturation.

The threshold value is adjusted manually and its value is set by means of visual examination. It is important to choose the correct threshold value to get a representative and accurate calculation. Failing to choose a proper threshold value affects the image analysis accuracy. For instance, Fig. 7 shows a comparison of an original image that was converted to black and white with two different threshold values. The porosity obtained changes correspondingly. The intensity versus frequency graphs show two humps where the left hump represents the high intensity pixels (oil) and the hump on the right side represents the low intensity pixels (water and grains).

5. Characterization results

The new micromodels were subjected to a variety of petrophysical characterization tests of increasing complexity. Porosity and permeability were examined first. These were followed by tests examining the connectivity and multiphase flow properties of the micromodel.
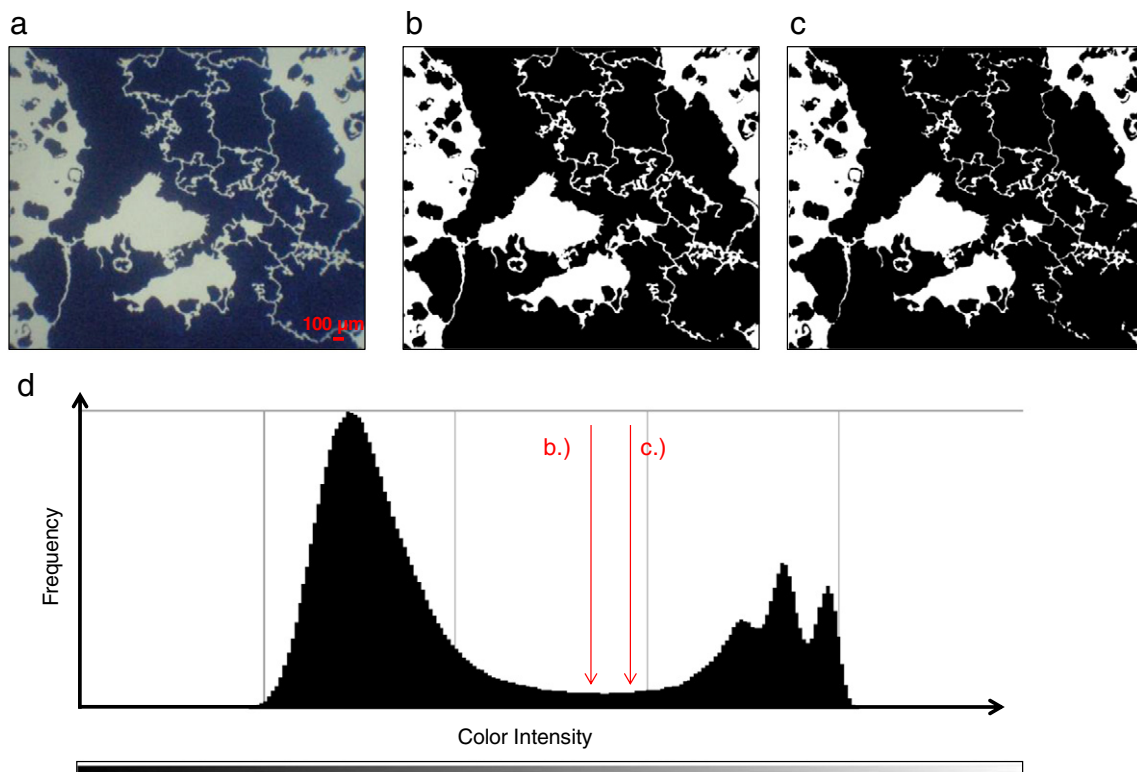

Fig. 7. (a) Black (grains) and white (voids) image in RGB mode; (b) Transformed black and white image with appropriate threshold value of 146 and a porosity of 40.5%; (c) Transformed black and white image with inappropriate threshold of 153 and a porosity of 38%; (d) Color intensity histogram of RGB picture with different threshold values of 146 (b) and 153 (c).

5.1. Porosity

The base image and the etched silicon wafer both have essentially an equal porosity of 45.5%, where pore structures equal to and smaller than 21 μm comprise about 25% of the total pore volume. As part of quality control procedures, micromodel porosities were measured to make sure that they exhibit good correlation with the mask porosity. Usually, micromodel porosity values determined by image analysis differ from mask porosity values. This discrepancy occurs because of the shadowing effects of the grains (Buchgraber et al., 2011). The shadowing effect tends to increase the number of the black pixels that then changes the porosity obtained. In order to remove the shadow effect, the carbonate micromodel was fully saturated with crude oil, the micromodel was illuminated with UV light, and pictures were taken for nine different positions inside one of the repeated patterns. The crude oil fluoresces under UV light providing excellent illumination and negates the shadowing effects observed under plain light. Eight pictures were taken and analyzed. The corresponding porosities averaged to 46%. As a result of being a dual-porosity carbonate micromodel, some areas exhibit very low porosity of 11% compared to some areas that exhibit high porosity values up to 74% (Fig. 8). This is a clear indication of dual porosity.

5.2. Permeability

One of the most important petrophysical properties to be determined for the carbonate micromodel is permeability. Several experiments were conducted to determine the micromodel permeability for different etching depths (4, 12, 14, 18, and 25 μm). The

permeability was interpreted using single-phase Darcy's law for incompressible (Eq. (1)) and compressible (Eq. (2)) flows, respectively:

$$k = \frac{q\mu L}{A(p_1 - p_2)} \tag{1}$$

$$k = \frac{2q\mu L p_b}{A(p_1^2 - p_2^2)}. \tag{2}$$

The experiments conducted to determine the permeability were done by one or two of the following approaches:

(1) The micromodel was flooded with distilled water at constant pressure and the corresponding flow rates measured; or, steady-state flow rates were imposed and corresponding pressure drop.
(2) The micromodel was flooded with CO_2 gas at various injection pressures and the corresponding flow rates measured via a bubble flow meter.
(3) The permeability value of each etching depth was averaged and plotted as shown in Fig. 9. The standard deviation of each measurement is about 35 mD.

5.3. Tracer test

A tracer test with water and water containing a UV-sensitive dye was performed in order to evaluate the main transport channels and check for complete access of injected fluid to all pore spaces. The model was first 100% saturated with distilled water and afterwards flooded with UV dyed water. As expected in a dual-porosity system, the larger interconnected pores that contribute most to the
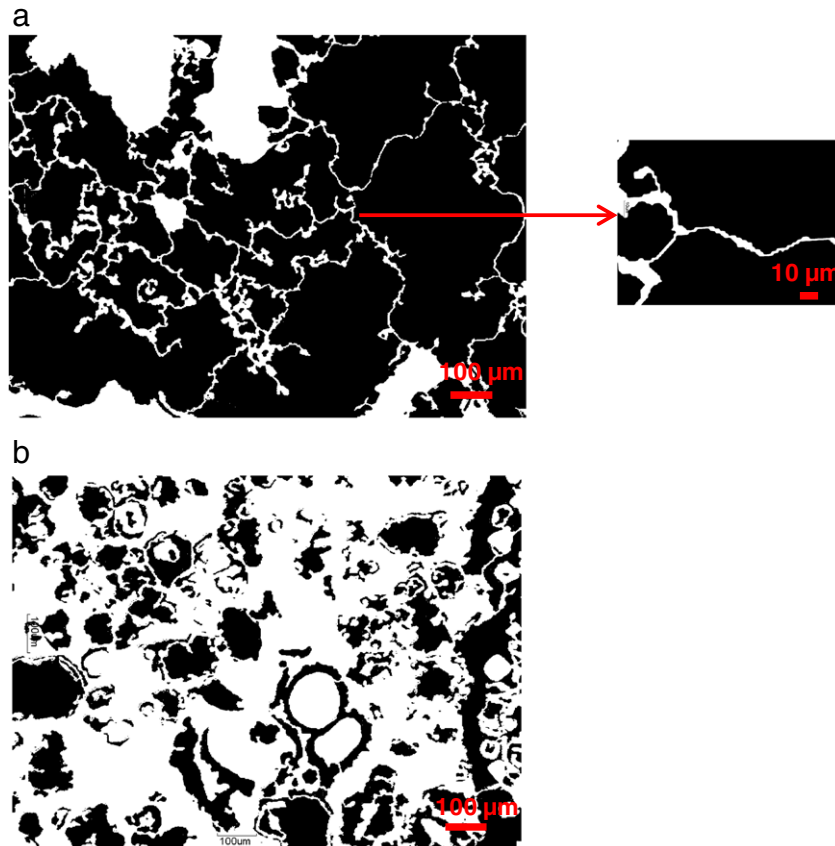

Fig. 8. Carbonate micromodel black (grains) and white (voids) images for two different regions that exhibit a wide range of porosity values, (a) regions of intragranular microporosity exist with 12% porosity, and (b) very porous areas with 74% porosity.
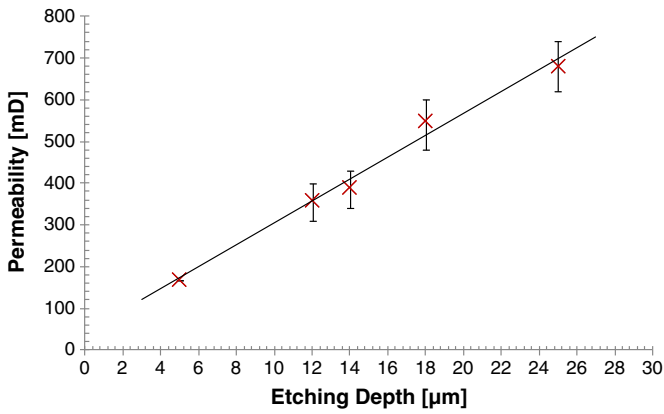
Fig. 9. Micromodel permeability versus etching depth.

fluid transport indicated the presence of tracer liquid first. Over time, the tighter microporous regions filled as shown in Fig. 10. After a total of 3 PV was injected, the entire micromodel was filled with tracer fluid.

5.4. Relative permeability

Relative permeability of oil and water is one of the major properties determining flow characteristics. Although the micromodel does not fully duplicate a 3D pore structure, measurement of relative permeability helps us understand flow processes and mechanisms better.

To obtain relative permeability curves for water, the model was first 100% saturated with crude oil followed by water imbibition at different
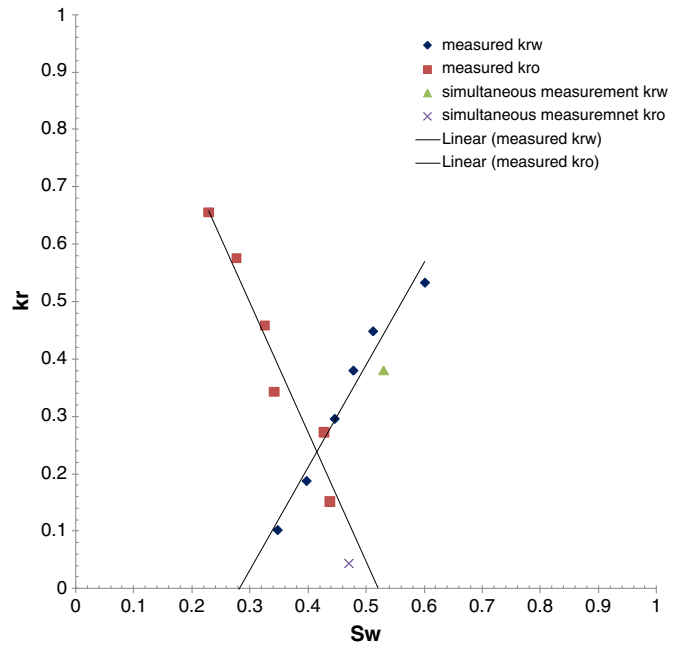

Fig. 11. Relative permeability curve for a 12 μm etch-depth micromodel.

pressures. Once the flow rate stabilized and steady-state conditions were achieved, pressure and rate were recorded and 25 micro saturation pictures were taken to determine the average saturation in the carbonate micromodel. Various pressure steps starting from 10 psi and going up to 120 psi, which is the maximum allowable pressure and at steady conditions also shows the irreducible water saturation, were
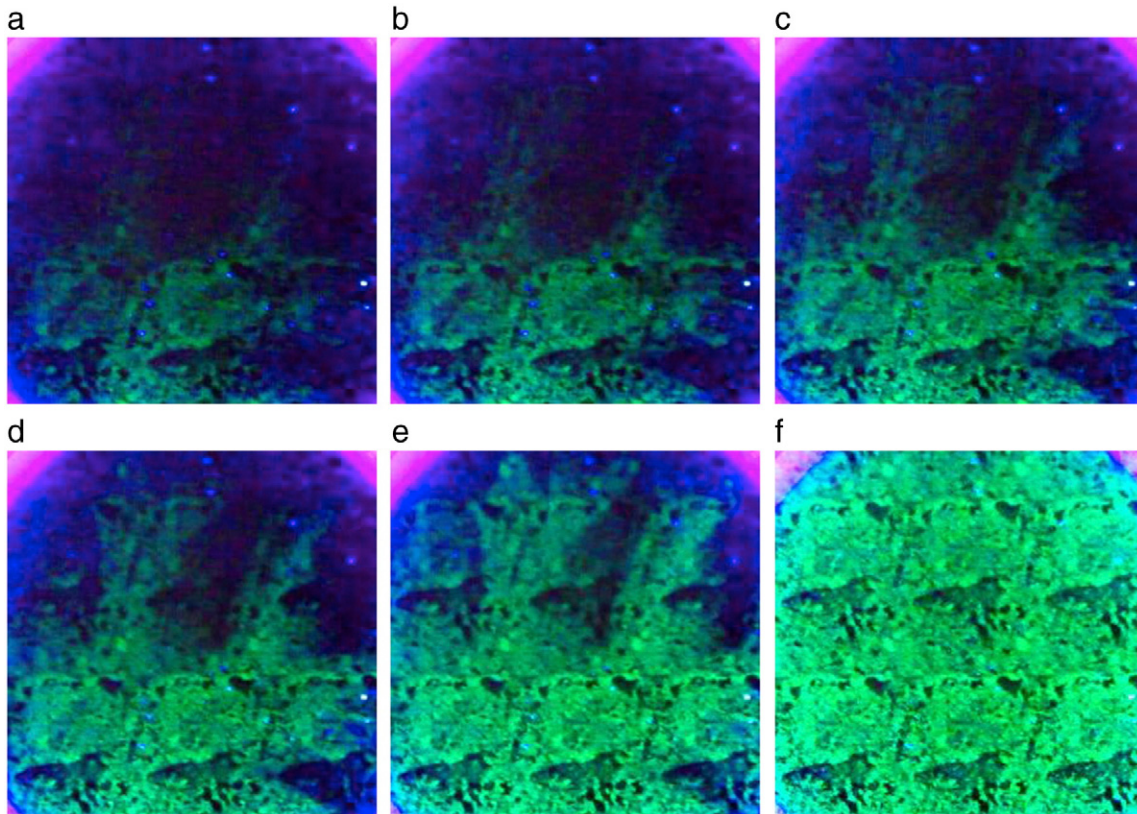

Fig. 10. Tracer test with distilled water (initial) and UV-dyed water (injected). Injection from the bottom: (a) 0.1 PV, (b) 0.2 PV, (c) 0.43 PV, (d) 0.62 PV, (e) 0.84 PV, and (f) 1.6 PV. Pore spaces fluoresce as they are filled with UV dye.
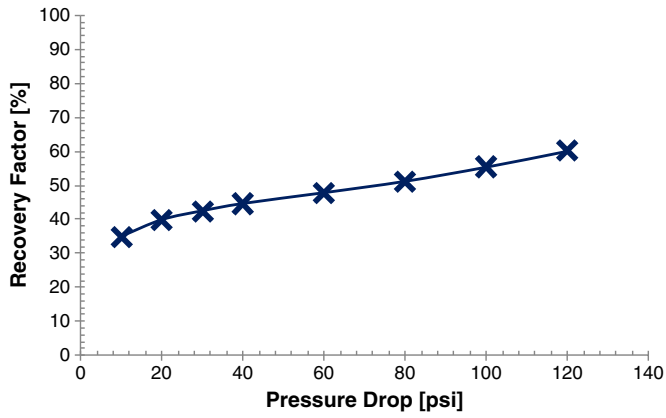
Fig. 12. Recovery factor versus pressure drop. Micromodel is sampled at four locations and recovery factor is averaged.

applied. Rate and pressure data were then used to calculate relative permeability according to the multiphase extension of Darcy's law:

$$k_{ri} = \frac{q_j \mu_j L}{A(p_1 - p_2)} \qquad (3)$$

where the subscript j refers to phase j. The same procedure was applied for the relative permeability of water except that the model was initially

100% saturated with water and a drainage process with oil was followed at the same pressure steps. In addition, a dynamic measurement was performed. Oil and water were injected simultaneously at the same rate. Once the pressure and micro saturation stabilized, pictures were taken and the pressure recorded. The dynamic measurement is in good agreement with the relative permeability measured above (Fig. 11).

The relative permeability curves obtained in Fig. 11 follow a straight line trend similar to what might be measured for a rough fracture (Rangel-German et al., 1999). That is, Corey exponents for oil and water equal to about 1 describe the micromodel. The intersection of k_{rw} and k_{ro} on the left side of the graph, Fig. 11, (S_w slightly less than 50%) is an indication of the oil-wet characteristic and is consistent with the visual observation of water in the center of pores shown in Fig. 6.

5.5. Recovery factor

After fully saturating the micromodel with oil, a water flood experiment at a constant injection rate of 0.0001 mL/min, which corresponds to a Darcy velocity of 1 ft/day, was conducted to determine the micromodel recovery factor. During the waterflood, several pictures were taken and analyzed. The saturation values were determined locally in order to be used for recovery factor calculations:

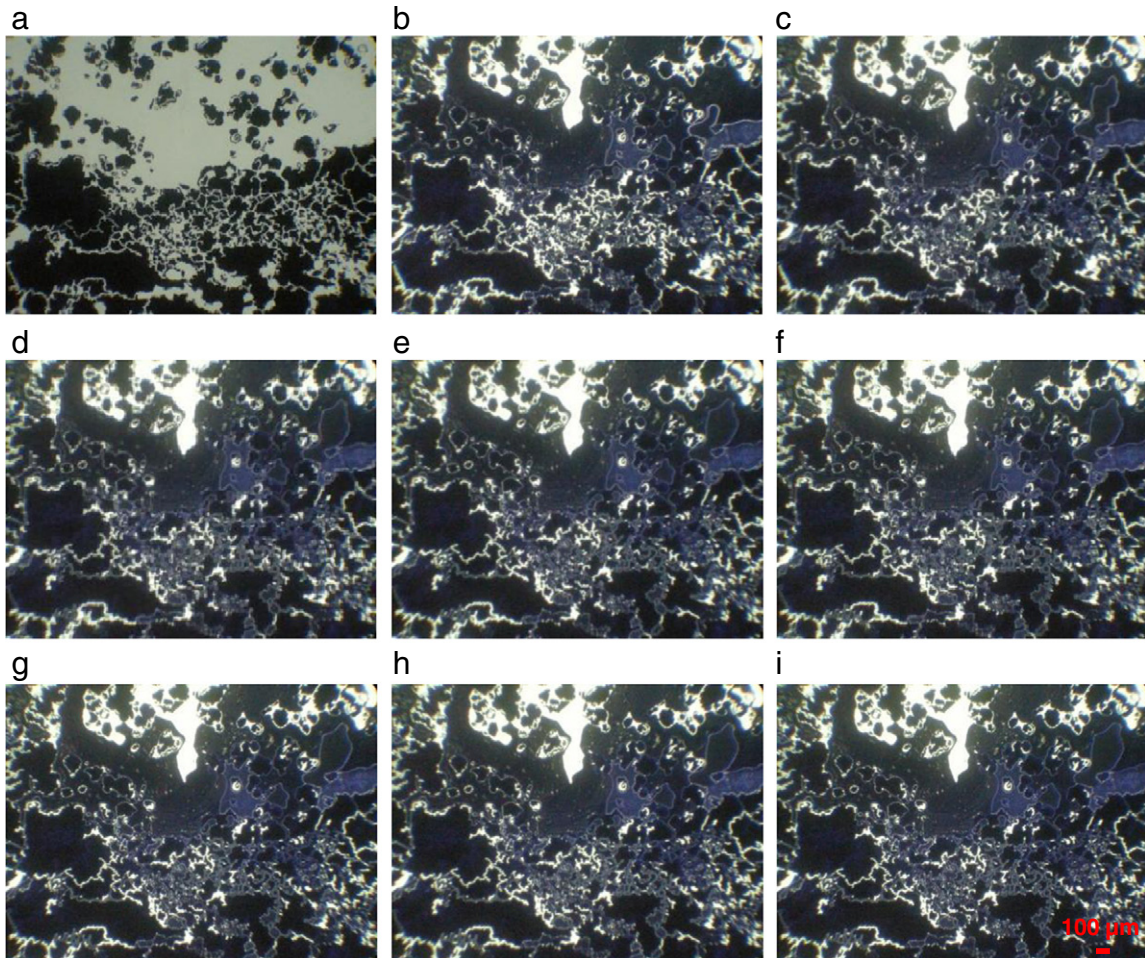$$R_f = \frac{S_{oi} - S_{or}}{S_{or}}. \qquad (4)$$

Fig. 13. Microsaturation pictures (white represents oil) at different /pressure drops across micromodel. a.) 100% oil saturated; b.) 10 psi − 71.1%; c.) 20 psi − 73.3.3%; d.) 40 psi − 74.8%; e.) 60 psi − 76%; f.) 80 psi − 76.4%; g.) 90 psi − 76.8%; h.) 110 psi − 77.1%; i.) 130 psi − 77.9%.
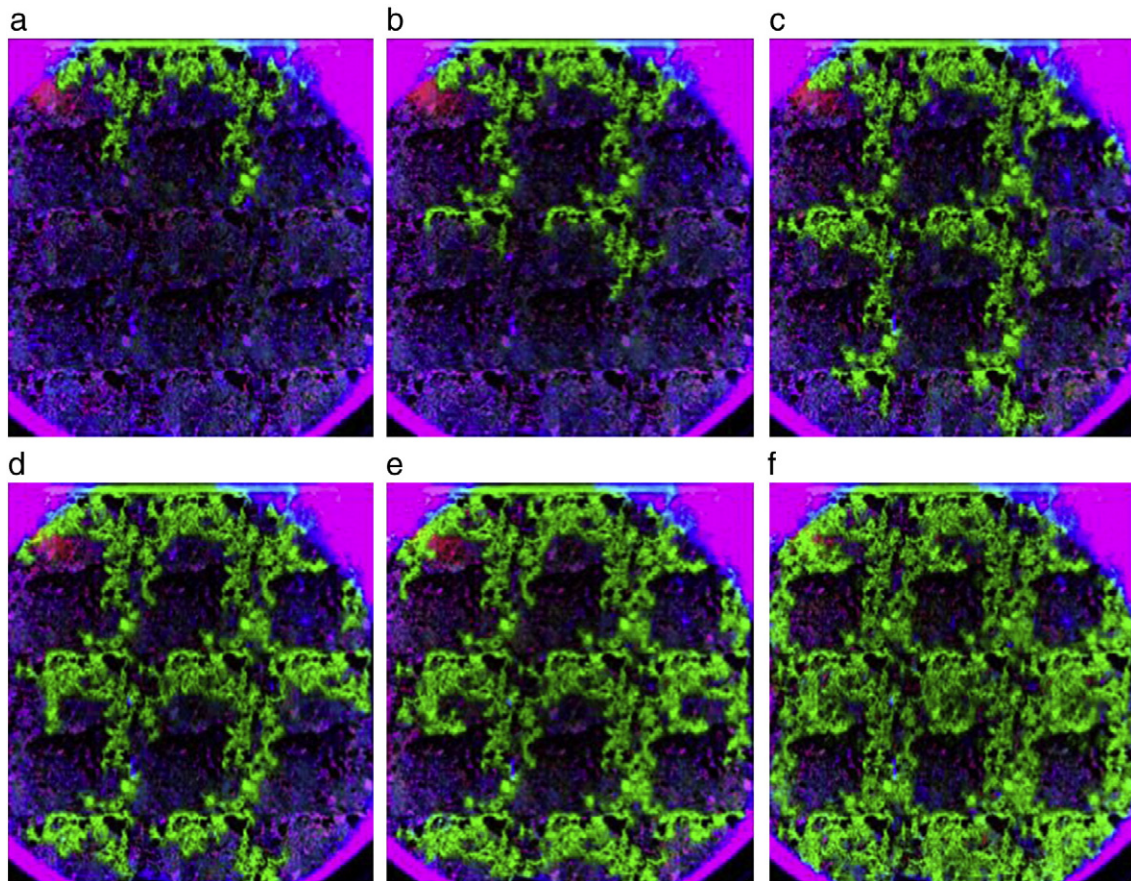
Fig. 14. Whole micromodel images of water displacing oil. The light source is circular and the edges of the micromodel are not imaged. The oil (7 cP) is shaded blue and pink. Water (1 cP) injection starts from the top at a Darcy velocity of 5 ft/day and follows the most permeable pathways. The water has a UV dye and is shaded green. Areal sweep efficiencies are a.) 12.7%, b.) 19.7%, c.) 42.3%, d.) 71%, e.) 84.4% and f.) 91%.
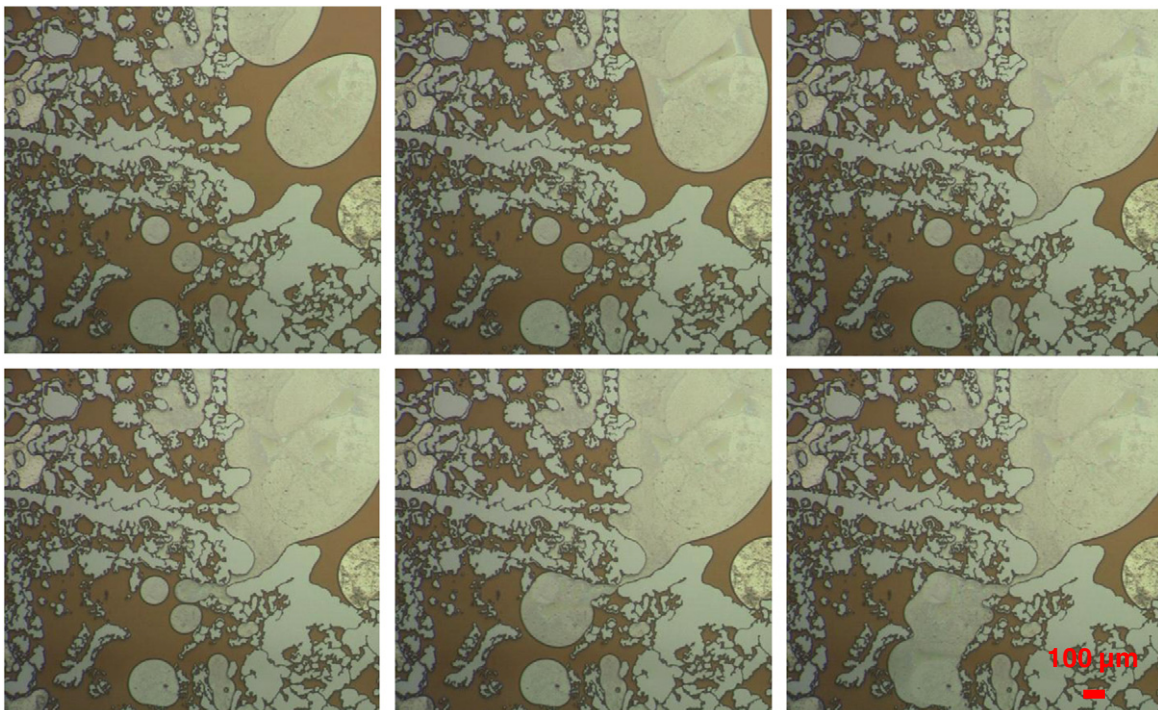

Fig. 15. Micro-scale images show injected water (clear) filling large pores and connecting with other water droplets; the time between the first and last image is about 190 s.

Several images with different spatial locations and time periods were used to find an average recovery factor of around 50%. Also, the results of the recovery factors as the injection pressure increased were analyzed. Here, water has been injected into the micromodel with a pressure of 10 psi. The pressure was then increased in 10 psi increments after a steady-state condition was established. Pictures from across the micromodel were taken, subjected to image analysis, and their corresponding recovery factors calculated (Figs. 12 and 13).

As expected, Fig. 12 shows that the greater the pressure drop across the micromodel during water injection, the more oil recovered. At lower pressures, larger pores were entered first as shown in Fig. 13. At pressure drops ranging from 80 to120 psi, smaller pores with greater capillary entry pressures were accessed and the oil displaced. An increase in recovery from 51 to 60% in the pressure range from 80 to 120 psi is accredited to the drainage of microporosity (Fig. 12). This 9% recovery increase indicates clearly the importance of microporosity. To complement this discussion of recovery and drainage of microporosity, observations of the progress of injected water across the entire micromodel were made as shown in Fig. 14. The injected water contains UV dye that aids in tracing the flow path of water. The slowly swept and unswept pore space is shown clearly and corresponds with regions of microporosity. After more than 3 PV of fluid injection the areal sweep of the micromodel approached 91%.

A similar drainage experiment was conducted at constant flow rate. Micro observations showed that microporosity could not be drained at low pressure drops (10–40 psi) even after multiple pore volumes (20 PV) were injected.

5.6. Displacement mechanism

During displacement processes, we noticed that the displacement mechanism occurring within the micromodel happened in two steps. Once the displacing fluid was injected, it tended to fill up the large pores whose capillary entry pressures were low (Fig. 14). Then, as the large pores were filled, the displacing fluid entered the next lowest capillary entry pressure pores until the large pores were connected. Furthermore, as the pore pressure builds up due to constant injection rate, smaller micropores were filled (Figs. 15 and 16). Figs. 15 and 16 show that displacement happened without the existence of the snap-off mechanism (Roof, 1970). Further work is needed to understand the generality of this observation. Due to the difficulty associated with analyzing images of the entire micromodel, no solid conclusion could be drawn regarding the overall flow pattern as well as the fingering behavior.

6. Summary

The construction and testing of a representative dual-porosity micromodel is described. This result was achieved by following a methodology based on converting an Arab-D proxy thin section into a binary image of the pore structure to use for mask creation. The resulting carbonate micromodel has an overall porosity of 46% with some regions having as low as 11% porosity and some areas having local porosity values as high as 74%. Clearly, a dual-porosity system is embodied in the micromodel. Also, the permeability of the micromodel as a function of different etch depths was determined. The five different depth micromodels showed permeability values ranging between 170 and 700 mD. Greater permeability was associated with greater etch depth, as expected. Recovery factors were found to be around 60%. Further investigation and scrutiny of the recovery factor as it relates to position will be conducted, because it was difficult to return to the exact locations that were used to determine the porosities and use them in the saturation calculations. Areas of high porosity with a vuggy pore structure and therefore a low capillary entry pressure showed greater recovery factors than areas dominated by microporosity with high capillary entry pressures.

This micromodel was developed for future studies to examine pore-level processes of enhanced oil recovery. The displacement studies
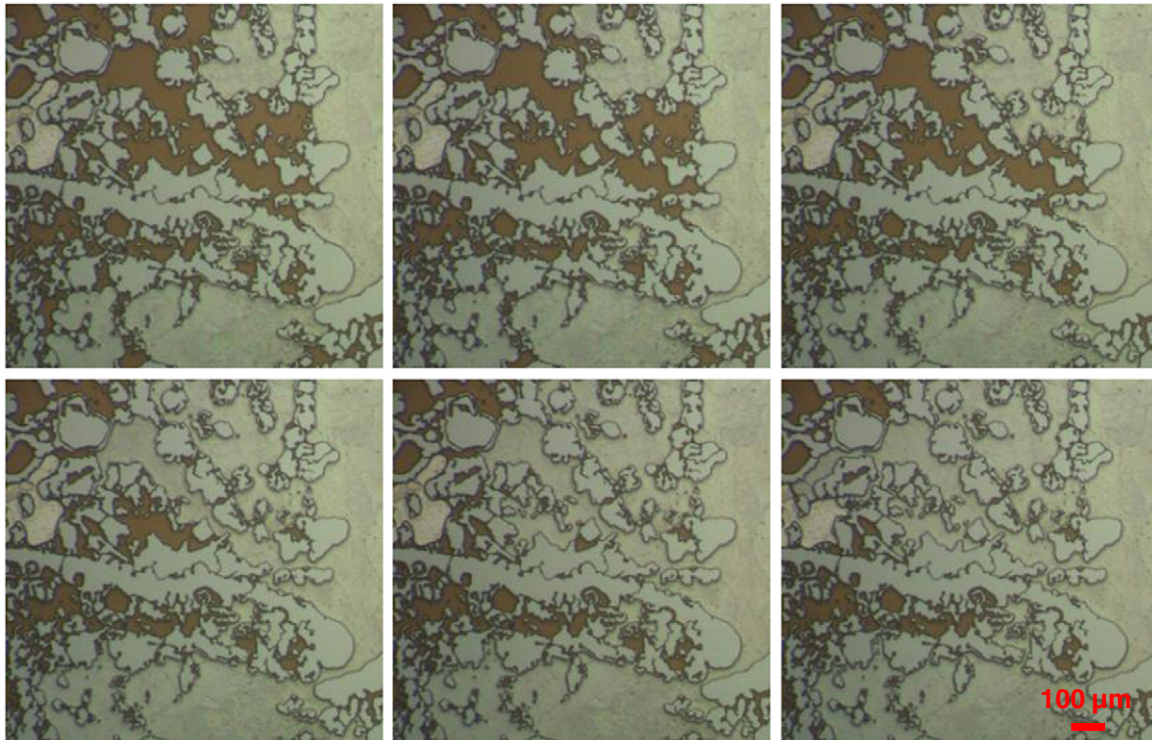

Fig. 16. Micro-scale images show injected water displacing oil from the small pores after the large pores have been swept; the time between the first and last image is around 310 s and images are equally spaced in time.

summarized here display the expected sequence of sweep of the more permeable and connected channels followed by a slower desaturation of the less permeable pore space. Little snap off of water under oil-wet conditions, and vice versa, is witnessed. The lack of oil recovery from microporosity at low waterflood rates and pressure drops leaves ample remaining oil in the micromodel consistent with dual porosity systems. A fraction of the remaining oil is recoverable, however, from the micromodel given a greater pressure drop. Accordingly, although held in microporosity, the remaining oil is a target for enhanced recovery using, for instance, surfactant laden injection water. The micromodel described is expected to allow visual observation of enhanced recovery mechanisms thereby improving understanding.

Nomenclature

A	cross-sectional area
k	permeability
k_{ri}	relative permeability of phase i
k_{ri}^*	endpoint relative permeability of phase i
L	length
p	pressure
p_b	base pressure
q	flow rate
R_f	recovery factor
S	phase saturation
μ	phase viscosity

Subscripts and superscripts

1	upstream
2	downstream
j	phase
o	oil phase
oi	original oil saturation
or	residual oil saturation
w	water phase
wi	initial water saturation
wr	residual water saturation

Acknowledgments

References

Buchgraber, M., Clemens, T., Castanier, L.M., Kovscek, A.R., 2011. A microvisual study of the displacement of viscous oil by polymer solutions. SPE Reserv. Eval. Eng. 14 (3), 269–280. doi:10.2118/122400-PA SPE-122400-PA.

Cantrell, Dave L, Hagerty, Royal M., 1999. Microporosity in Arab formation carbonates, Saudi Arabia. GeoArabia 4, 129–150.

Chambers, K.T., Radke, C.J., 1991. 1989. Capillary phenomena in foam flow through porous media. In: Morrow, N.R. (Ed.), Interfacial Phenomena in Petroleum Recovery. Marcel Dekker Inc., New York, pp. 191–255.

Chilinger, G.V., Yen, T.F., 1983. Some notes on wettability and relative permeabilities of carbonate reservoir rocks II. Energy Sources 7, 67–75.

Choquette, P.W., Pray, L.C., 1970. Geological nomenclature and classification of porosity in sedimentary carbonates. Am. Assoc. Pet. Geol. Bull. 54, 207–250.

Clerke, E.A., 2009. Permeability, relative permeability, microscopic displacement efficiency and pore geometry of M_1 bimodal pore bystems in Arab-D limestone. Soc. Pet. Eng. J. 14 (3), 524–531.

Davis Jr., J.A., Jones, S.C., 1968. Displacement mechanisms of micellar solutions. JPT, SPE-1847. . (Dec).

George, D. S. 1999. Visualization of solution gas drive in viscous oil, Stanford University, M.S. Thesis. ekofisk.stanford.edu/theses

George, D.S., Hayat, O., Kovscek, A.R., 2005. A microvisual study of solution gas drive mechanisms in viscous oils. J. Pet. Sci. Eng. 46 (1–2), 101–119. doi:10.1016/j.petrol.2004.08.003.

Hornbrook, J.W., Castanier, L.M., Petit, P.A., 1991. Observation of foam/oil interactions in a new, high-resolution micromodel. SPE 22631, SPE Annual Technical Conference and Exhibition, Dallas, Texas.

Kovscek, A.R., Wong, H., Radke, C.J., 1993. A pore-level scenario for the development of mixed wettability in oil reservoirs. Am. Inst. Chem. Eng. J. 39 (6), 1072–1085.

Mattax, C.C., Kyte, J.R., 1961. Ever see a water flood. Oil Gas J. 115–128 (Oct).

McKellar, M., Wardlaw, N.C., 1982. A method of making two-dimensional glass micromodels of pore systems. J. Can. Pet. Technol. 21 (4), 39–41.

Neinhuis, C., Barthlott, W., 1997. Characterization and distribution of water-repellent self-cleaning plant surfaces. Ann. Bot. 79 (6), 667–677.

Oren, P.E., Billiotte, J., Pinczewski, W.V., 1992. Mobilization of waterflood residual oil by gas injection for water-wet conditions. Soc. Pet. Eng. Form. Eval. 7 (1), 70–78.

Petricola, M.J.C., Watfa, M., 1995. Effect of microporosity in carbonates: introduction of a versatile saturation equation. SPE 29841. Middle East Oil Show, Bahrain.

Pittman, E.D., 1971. Microporosity in carbonate rocks. Am. Assoc. Pet. Geol. Bull. 55, 1873–1881.

Rangel-German, E.R., Kovscek, A.R., 2006. A micromodel investigation of two-phase matrix-fracture transfer mechanisms. Water Resour. Res. 42 (W03401). doi:10.1029/2004WR003918.

Rangel-German, E.R., Akin, S., Castanier, L.M., 1999. Multiphase flow properties of fractured porous media. J. Pet. Sci. Eng. 51 (3–4), 197–213.

Rao, A., Latthe, S., Dhere, S., Pawar, S., Imai, H., Ganesan, V., Gupta, S., Wagh, P., 2010. Control on wetting properties of spin-deposited silica films by surface silylation method. Appl. Surf. Sci. 256, 2115–2121.

Roof, J.G., 1970. Snap-off of oil droplets in water-wet pores. Soc. Pet. Eng. J. 10, 85–90.

Ross, C.M., Callender, C.A., Turbeville, J.B., Funk, J.J., 1995. Modeling of capillary pressure behavior using standard open hole wireline log data demonstrated on carbonates from the Middle East. Paper SPE 30543 Presented at the SPE Annual Technical Conference and Exhibition, Dallas, pp. 22–25.

US Energy Information Administration (US EIA), 2011. Country Analysis Saudi Arabia (January). http://www.eia.gov/countries/cab.cfm?fips=SA2011accessed Nov 8, 2011.